

Twist-angle evolution from valley-polarized fractional topological phases to valley-degenerate superconductivity in twisted bilayer MoTe₂

Zheng Sun^{1†}, Fan Xu^{1,2†}, Jiayi Li^{1†}, Yifan Jiang^{3†}, Jingjing Gao^{4,8,9†}, Cheng Xu^{5,10†}, Tongtong Jia¹, Kehao Cheng¹, Jinyang Zhang⁴, Wanghao Tian¹, Kenji Watanabe⁶, Takashi Taniguchi⁷, Jinfeng Jia^{1,2,8,9}, Shengwei Jiang^{1,2}, Yang Zhang^{5,11}, Yuanbo Zhang^{4,8,9,12*}, Shiming Lei^{3*}, Xiaoxue Liu^{1,2,8,9*}, and Tingxin Li^{1,2,8*}

¹State Key Laboratory of Micro-nano Engineering Science, Key Laboratory of Artificial Structures and Quantum Control (Ministry of Education), School of Physics and Astronomy, Shanghai Jiao Tong University, Shanghai, China

²Tsung-Dao Lee Institute, Shanghai Jiao Tong University, Shanghai, China

³Department of Physics, Hong Kong University of Science and Technology, Clear Water Bay, Hong Kong SAR, China

⁴State Key Laboratory of Surface Physics and Department of Physics, Fudan University, Shanghai, China

⁵Department of Physics and Astronomy, University of Tennessee, Knoxville, TN, USA

⁶Research Center for Electronic and Optical Materials, National Institute for Materials Science, 1-1 Namiki, Tsukuba, Japan

⁷Research Center for Materials Nanoarchitectonics, National Institute for Materials Science, 1-1 Namiki, Tsukuba, Japan

⁸Hefei National Laboratory, Hefei, China

⁹Shanghai Research Center for Quantum Sciences, Shanghai, China

¹⁰Max Planck Institute for Chemical Physics of Solids, Dresden, Germany

¹¹Min H. Kao Department of Electrical Engineering and Computer Science, University of Tennessee, Knoxville, Tennessee, USA

¹²New Cornerstone Science Laboratory, Department of Physics, Fudan University, Shanghai, China

[†]These authors contribute equally to this work.

*Emails: zhyb@fudan.edu.cn, phslei@ust.hk, xxliu90@sjtu.edu.cn, txli89@sjtu.edu.cn

Abstract:

Moiré superlattices formed by semiconducting transition metal dichalcogenides (TMDs) provide a highly tunable platform for investigating strongly correlated and topological quantum phases [1-4]. As a prototypical example, twisted bilayer MoTe₂ (tMoTe₂) has been shown to host fractional topological phases [5-22], such as zero-field fractional Chern insulators (FCIs) exhibiting fractional quantum anomalous Hall (FQAH) effects.

However, how these correlated topological phases evolve with twist angle and compete with other quantum phases in tMoTe₂ remains largely unexplored. Here we report a systematic transport study of twist-angle-dependent phase diagrams in tMoTe₂ across a range of 3.8°–5.78°, revealing an evolution from fractionalized states of matter with spontaneous valley polarization to valley-degenerate superconductivity. At relatively small twist angles, partially-filled Chern bands of tMoTe₂ host FQAH states following the Jain sequence, together with signatures of an anomalous composite Fermi liquid at moiré hole filling factor $\nu_h = 1/2$. Increasing twist angle progressively suppresses fractional topological phases and reconstructs the half-filled Chern band into symmetry-breaking integer Chern insulating states. At $\nu_h = 1$, we observe a transition from robust integer quantum anomalous Hall (IQAH) insulators at small angles to displacement-field-tuned, topologically trivial correlated insulators at larger angles. Remarkably, at a twist angle of 5.78°, superconductivity emerges adjacent to the correlated insulating phase, with a phase diagram closely resembling that recently reported in twisted bilayer WSe₂ (tWSe₂) [23-26]. Our results uncover a unified twist-angle-driven phase evolution linking fractional topology, symmetry breaking, magnetic order, and superconductivity, providing new insight into the emergent quantum phenomena in moiré systems.

Main:

Twisted semiconducting TMD homobilayers have emerged as a model platform that is both theoretically tractable and experimentally rich, enabling systematic exploration of correlated and topological quantum phenomena. Within a continuum-model framework [27-30], the low-energy moiré valence bands at the *K*-valley of tMoTe₂ and tWSe₂ are predicted to be similar, both supporting topologically nontrivial moiré flat bands that effectively emulate the Kane–Mele model [31]. These topological flat bands are highly tunable: an applied vertical electric field can induce layer polarization and therefore drives a transition toward a topologically trivial regime. Furthermore, the band topology and associated quantum phases are also predicted to be sensitive to the twist angle [32-45]. Subsequent experiments revealed a rich variety of quantum phases in these systems, including zero-field integer and fractional Chern insulators [5-8], quantum spin Hall insulators [18], and superconductivity [15,23-26].

However, experiments have revealed a clear distinction in the emergent phase diagrams of the two systems. In tMoTe₂, previous studies uncovered robust ferromagnetism together with integer and fractional Chern insulating states over a broad twist-angle range of 2.1°–3.9° [5-17]. More recently, in high-quality tMoTe₂ devices around 3.83°, reentrant quantum anomalous Hall (RQAH) states and superconductivity are observed in close proximity to FQAH phases, where the superconducting state develops from a valley-polarized Fermi surface exhibiting an anomalous Hall (AH) response [15]. In

contrast, tWSe₂ displays zero-field integer Chern insulating states only within a narrow window below $\sim 2^\circ$ [46,47], although itinerant ferromagnetism persists up to $\sim 2.7^\circ$ [48]. And so far, no FCIs or other fractional topological phases has been observed in tWSe₂. Instead, robust superconductivity has been observed in tWSe₂ at larger twist angles between approximately 3.5° and 5° [23-26], arising from a valley-degenerate Fermi surface and are considered to be associated with intervalley-coherent antiferromagnetic (AFM) order [49-59]. The origin of these striking differences between otherwise theoretically analogous moiré TMD systems remains unclear. And a systematic experimental study of how fractional topology, magnetic order, and emergent superconductivity evolve across twist angle has remained lacking.

Here we address this question by systematically mapping the transport phase diagram of tMoTe₂ across eleven high-quality devices (see Extended Data Fig. 1 for device summary), covering a twist-angle range of 3.8° – 5.78° . The twist angle θ is calibrated through quantum oscillations under magnetic fields (Extended Data Fig. 2). Most devices were fabricated using high-quality, flux-grown 2H-MoTe₂ single crystals (Methods).

Twist-angle-dependent phase diagram in tMoTe₂

Figure 1a shows a schematic of the tMoTe₂ device used for transport measurements (Methods). Figure 1b presents the calculated density of states (DOS) as a function of interlayer potential difference Δ and ν_h , for 5.8° tMoTe₂ as an example (Methods). The Δ can be induced by the applied vertical electric field. At zero electric field, the van Hove singularity (VHS) lies below $\nu_h = 1$, and it shifts to higher ν_h with increasing Δ . By varying the θ between adjacent layers, the moiré wavelength and the resulting electronic bandwidth can be continuously tuned, as shown in Fig. 1c. Figure 1d-1i present the longitudinal resistivity ρ_{xx} as a function of ν_h and vertical displacement electric field D , measured at temperature $T = 1.6$ K under a perpendicular magnetic field of $B = 0.1$ T (or 0 T) for six representative tMoTe₂ devices (also see Fig. 2g, 3a, 3c, and Extended Data Fig. 3 of similar maps for five additional devices), with θ ranging from 3.8° to 5.78° . For devices with θ smaller than approximately 4° , the ρ_{xx} phase diagram closely resembles those reported previously [7,8,12-15]. Specifically, in the layer-hybridized regime, vanishing ρ_{xx} around $D = 0$ signals the formation of interaction-induced valley-polarized Chern insulating states, including the IQAH state at $\nu_h = 1$, and FQAH states at $\nu_h = 2/3$, $3/5$, and $4/7$. In the layer-polarized regime, pronounced insulating states driven by strong electron-electron interactions emerge at $\nu_h = 1$, $2/3$, $1/2$, $1/3$, and $1/4$. These states are topologically trivial, and can be understood as a Mott insulating state ($\nu_h = 1$) and generalized Wigner crystal states on the triangular moiré superlattice [1,2].

As the θ increases, both IQAH and FQAH states in the layer-hybridized region are gradually suppressed. The corresponding ρ_{xx} minima weaken and eventually disappear, reflecting a gradual destabilization of chiral edge transport. For devices with θ exceeding approximately 5° , no signatures of magnetic hysteresis are detected at any fillings, demonstrating the fully suppression of spontaneous valley polarization. Instead, only weak insulating features remain in the layer-hybridized regime, particularly at $\nu_h = 1$ and $1/2$. Taken together, these observations demonstrate a systematic twist-angle-driven evolution from a strongly interacting, valley-polarized topological regime at small angles to a more itinerant and valley-degenerate regime at larger angles.

The weakening of electronic interactions with increasing θ is further evident by the evolution of topologically trivial correlated insulating states in the layer-polarized regime. With increasing θ , the correlated insulating states in the layer-polarized region become significantly weakened, consistent with an increased bandwidth and a reduced interaction-to-kinetic-energy ratio. Phenomenologically, we observe that these layer-polarized correlated insulating states disappear sequentially with increasing θ , following the order of $\nu_h = 1/4, 1/3, 2/3, 1/2$, and finally 1. In addition, for small-angle devices and near $D = 0$, a broad insulating region emerges that is continuous in filling factor: for θ below approximately 4.5° , the system remains insulating for roughly $\nu_h < 0.4$ around $D = 0$ (Fig. 1d-g). As the twist angle increases, this continuous insulating regime progressively shrinks. By 5.78° , only discrete insulating states at $\nu_h = 1/4, 1/3$ remain, with the intervening fillings becoming metallic (Fig. 1i).

The evolution of FQAH and ACFL phases with twist angles

Next, we investigate the evolution of fractional topological phases in partially-filled Chern bands as a function of θ . The interplay between strong correlations and nontrivial topology within a flat Chern band provides a fertile ground for investigating exotic quantum phases. Among them, FCIs represent interaction-driven incompressible states characterized by fractionally quantized anomalous Hall conductance in the absence of magnetic field. Moreover, at half filling of a flat Chern band, theory predicts the emergence of an anomalous composite Fermi liquid (ACFL) [32,33], a compressible metallic state formed by composite fermions at zero magnetic field.

Figure 2a-2e show the symmetrized ρ_{xx} and antisymmetrized Hall resistivity ρ_{xy} as a function of ν_h at $D = 0$ and $B = 0.1$ T for device 1-4 and 6, respectively. For device 1 with $\theta = 3.8^\circ$, three prominent FQAH states are observed at $\nu_h = 2/3, 3/5$, and $4/7$, following the Jain sequence. These states exhibit pronounced local minima in ρ_{xx} accompanied by quantized anomalous Hall plateaus in ρ_{xy} (Fig. 2a,g,h), consistent with previous studies [7,8,12-15]. Notably, at $\nu_h = 1/2$, the AH resistivity approaches $2h/e^2$ but without a plateau feature in ρ_{xy} and a local minimum in ρ_{xx} , demonstrating a

compressible nature of the state. Theoretically, a compressible state with AH response close to $2h/e^2$ at half-filled Chern band, together with the emergence of FQAH states following Jain-sequence at partially-filled Chern band constitutes a hallmark of an ACFL rather than a conventional Fermi liquid [32-35]. Recent optical measurements have provided further support for the existence of such ACFL phases [17].

As the θ increases, the number of observable FQAH states gradually decreases. At $\theta = 4.05^\circ$ (device 3), only the $\nu_h = 2/3$ FQAH state remains, and its ρ_{xy} already significantly deviate from the quantized value of $3h/2e^2$. Upon further increasing the twist angle to $\theta = 4.15^\circ$, all FQAH states disappear, although ferromagnetic order still persists over the filling range of $\nu_h \approx 1/2$ to 1 at $D = 0$ (see Extended data Fig. 4). Meanwhile, the AH resistivity at $\nu_h = 1/2$ drops below $2h/e^2$ with increasing θ , demonstrating the destabilization of the ACFL phase. Notably, in devices with θ between 4.15° and 4.68° , integer Chern insulating states emerge at fractional ν_h , spontaneously breaking the translational symmetry of the underlying moiré superlattice. Specifically, in device 4 ($\theta = 4.15^\circ$), we observe an integer-quantized anomalous Hall plateau of h/e^2 in ρ_{xy} , accompanied by a local minimum in ρ_{xx} , centered at $\nu_h \approx 0.62$ (Fig. 2d,i,j). For device 6 ($\theta = 4.55^\circ$) and device 7 ($\theta = 4.68^\circ$), integer Chern insulating states appear at $\nu_h = 1/2$, as shown in Fig. 2e,k,l and Extended Data Fig. 5-7. These observations suggest a twist-angle-driven topological phase transition at half-filled Chern band, in which the compressible ACFL gives way to symmetry-broken integer Chern insulating (SBCI) phases (or equivalently interpretable as topological charge density waves), consistent with recent theoretical calculations [34]. Figure 2f summarize the evolution of the AH resistivity as a function of θ at $\nu_h = 2/3$ and $1/2$. Both signals collapse rapidly once θ exceeds $\sim 4.0^\circ$, marking the disappearance of fractional topological phases, while an intermediate SBCI state emerges at $\nu_h = 1/2$ before the valley polarization is fully suppressed.

QAH insulator, correlated insulator and superconductivity at $\nu_h = 1$

We next focus on the twist-angle evolution of correlated and topological phases at $\nu_h = 1$. As shown in Fig. 1d-f, 2g-j, and Extended Data Fig. 3, for devices with $\theta < 4.25^\circ$ (device 1-5), robust IQAH states are observed over a continuous range of displacement electric field around $D = 0$, while topologically trivial correlated insulating states appear in the layer-polarized regime at larger D . These observations are consistent with previous reports [7,8,11-15]. Interestingly, in device 6 (4.55°) and 7 (4.68°), we noticed that the IQAH state at $\nu_h = 1$ no longer exists at $D = 0$ but instead emerges only at finite D , as shown in Fig. 2k,l and 3a,b. Notably, the emergence of IQAH states roughly coincides with the D -field at which the single-particle VHS crosses $\nu_h = 1$ (Extended Data Fig. 8). The Curie temperature for the ferromagnetism at $\nu_h = 1$ in device 6 (4.55°) and 7 (4.68°) is approximately 3-4 K (Extended Data Fig. 5, 6),

significantly lower than the values previously observed at smaller θ [7,8,14] (~ 10 -15 K in 3.5° - 4° devices). Such reduction reflects the weakening of interaction effects with increasing θ . Above the Curie temperature, the transport behavior at $\nu_h = 1$ in the layer-hybridized regime becomes metallic (Fig. 3b).

With further increasing θ to around 5° , both the IQAH state at $\nu_h = 1$ and ferromagnetism at other fillings are completely suppressed. Figure 3c shows ρ_{xx} as a function of ν_h and D for device 9 (5.0°). Although ρ_{xx} features within the layer-hybridized region remain qualitatively similar to those observed in device 7 (4.68°), a topologically trivial correlated insulating state appears instead of the IQAH insulator at comparable D values where the VHS crosses $\nu_h = 1$. The activation gap of the correlated insulating state at $\nu_h = 1$, extracted from the T -dependent ρ_{xx} (Fig. 3d), is approximately 2 meV.

Figure 3e displays ρ_{xx} as a function of ν and D for device 11 (5.78°), measured at a nominal base $T = 10$ mK (Methods) and $B = 0$ T. At this larger twist angle, correlation effects are further weakened. Aside from the correlated insulating states at $\nu_h = 1/4$ and $1/3$ near $D = 0$, together with the $\nu_h = 1$ insulating state and nearby features at finite D , most remaining transport features can be well captured by a single-particle band framework. Remarkably, superconductivity emerges in close proximity to the correlated insulating state at $\nu_h = 1$, as discussed in the next section.

Theoretical calculations [37-44] have suggested that at $\nu_h = 1$, twisted TMD homobilayers host a hierarchy of competing interaction-driven phases with various magnetic orders, whose stability is controlled by θ and D . In the layer-hybridized regime, calculations predict a multiferroic phase with spontaneous layer polarization and magnetism at very small θ , a valley-polarized quantum anomalous Hall insulator with Chern number $C = 1$ at intermediate θ , and topologically trivial AFM orders at larger θ , where increased bandwidth and reduced topological character suppress valley polarization. The evolution of the latter two regimes with θ is in qualitative agreement with our experimental observations, as summarized in the experimental phase diagram shown in Fig. 3f. Moreover, the fact that insulating states at $\nu_h = 1$ in large-twist-angle ($\theta > 4.5^\circ$) devices emerge only when the VHS approaches filling $\nu_h = 1$ illustrates that the enhanced DOS associated with the VHS amplifies interaction effects and promotes fully-gapped insulating phases, either topologically nontrivial or trivial, over metallic phases.

Superconductivity in 5.78° tMoTe₂

Figure 4 further illustrates the characteristics of the superconducting states emerging near $\nu_h = 1$ in 5.78° tMoTe₂ (device 11). The finely scanned local map (Fig. 4a) reveals that superconductivity develops adjacent to the low $|D|$ end of the $\nu_h = 1$ correlated

insulator and becomes most robust at fillings slightly below $\nu_h = 1$ (Extended Data Fig. 9). Figure 4b shows the ρ_{xx} as a function of D and T at $\nu_h = 1$, where insulating, superconducting, and metallic behaviors appear sequentially with decreasing D in the layer-hybridized regime. Representative ρ_{xx} - T curves shown in Extended Data Fig. 10 illustrate the transport characteristic for these three regions. In the insulating region, an energy gap of approximately 2 meV is extracted. In the superconducting region, the normal state exhibits strange-metal behavior, whereas the metallic region at smaller $|D|$ follows Fermi-liquid behavior.

Figure 4c presents the ρ_{xx} as a function of ν_h and T cut across the optimal superconducting region, with the optimal superconducting transition temperature T_c about 225 mK (determined by 50% normal resistivity R_n). This is further evident by the measured differential resistivity dV/dI as a function of the dc bias current I_{dc} (Fig. 4d). Figure 4e shows dV/dI as a function of B at $T = 10$ mK, from which a perpendicular critical magnetic field $B_c \approx 100$ mT can be identified. Figure 4f shows the ρ_{xx} - T curves measured under different B at optimal ν_h and D for the superconducting state. From a Ginzburg–Landau analysis of the temperature dependence of B_c (inset of Fig. 4f), the superconducting coherence length is estimated to be $\xi \approx 44$ nm (Methods). The 5.78° twist angle corresponds to a moiré wavelength of $a_M \approx 3.5$ nm, and the mean free path in this device is estimated to be $l_m \approx 120$ nm (Methods). These values indicate relatively tightly bonded Cooper pairs ($\xi/a_M \approx 12.5$), and suggest that the superconductor is in the clean limit ($\xi/l_m \approx 0.37$).

Phenomenologically, the observed superconducting characteristic and phase diagram in 5.78° tMoTe₂ recall the recent reported superconductivity in tWSe₂, especially for those devices around 4.3° [25,26]. Current theories [49-59] generally attribute superconductivity in tWSe₂ to electronically mediated pairing emerging from the interplay of strong correlations and nontrivial band topology. Fluctuations associated with nearby symmetry-broken or correlated insulating phases—particularly intervalley-coherent AFM order or quantum critical fluctuations—are widely considered the primary pairing mechanism, giving rise to unconventional and potentially topological superconductivity. The observation of analogous superconductivity in large-angle tMoTe₂ therefore provides an important opportunity to clarify the microscopic origin of this class of moiré superconductors through direct comparison between different material platforms.

Discussions and conclusions

In this work, we address how tMoTe₂ evolves from a regime dominated by valley-polarized fractional topological order to one supporting valley-degenerate superconductivity. At large twist angles, the transport phase diagrams of tMoTe₂ and

tWSe₂ become remarkably similar, with valley-degenerate superconductivity emerging near the $\nu_h = 1$ correlated insulating state within the layer-hybridized regime. In general, tMoTe₂ exhibits stronger correlation effects at comparable moiré wavelengths, likely due to the larger effective mass of monolayer MoTe₂ ($\sim 0.75 m_0$) [60] compared with that of monolayer WSe₂ ($\sim 0.4 m_0$) [61,62]. For example, although 5.0° tWSe₂ ($a_M \approx 3.8$ nm) and 5.78° tMoTe₂ ($a_M \approx 3.5$ nm) possess similar moiré wavelength, correlated insulators are absent in 5.0° tWSe₂ but remain robust in 5.78° tMoTe₂. On the other hand, the superconducting transition temperature is higher in 5.0° tWSe₂.

As the θ decreases and electronic correlations strengthen in both systems, their phase evolution diverges significantly. In tWSe₂, ferromagnetism and QAH states are difficult to stabilize; even at 2.7° , only trivial correlated insulating behavior has been reported at $\nu_h = 1$ and $B = 0$ [48]. By contrast, 4.68° tMoTe₂ already hosts IQAH states at $\nu_h = 1$ and SBCI states at $\nu_h = 1/2$. In devices with $\theta < 4.05^\circ$, fractional topological phases including FQAH and ACFL states further emerge. The competition among fractional topological ground states across θ may be understood from a quantum-geometric perspective: although correlations at relative large angles ($\sim 4.0^\circ$ - 4.7°) are still sufficient to induce valley polarization in tMoTe₂ at fractional moiré fillings, deviations from ideal quantum geometry likely prevent FCIs and ACFL from becoming the ground state [63-65].

Our results suggest that superconductivity in tMoTe₂ may fall into two distinct classes. At small angles, as reported previously [15], unconventional superconductivity coexists with fractional topological phases and emerges from a valley-polarized normal state. At large twist angles, as demonstrated in current work, valley polarization is fully suppressed and superconductivity instead develops from a valley-degenerate Fermi surface, while no superconductivity has been observed at intermediate angles thus far. A systematic understanding of how superconductivity, and its underlying pairing mechanism, evolves with twist angle in tMoTe₂ therefore remains an important open question. Our results uncover a rich twist-angle-dependent landscape of quantum phases in tMoTe₂, and provide a fascinating platform for investigating how unconventional superconductivity emerges from competing correlated and topological electronic states.

Methods

2H-MoTe₂ Crystal growth

High-quality 2H-MoTe₂ single crystals were synthesized independently at Hong Kong University of Science and Technology (HKUST) and Fudan University (FDU).

Although the detailed growth parameters differ slightly, both approaches follow similar tellurium-rich flux growth procedures. The growth recipes used at HKUST and FDU are described below.

HKUST: High-quality MoTe₂ single crystals were synthesized using an optimized vertical self-flux method. Molybdenum powder (99.997% Mo) and excess tellurium blocks (99.99999% Te) were thoroughly mixed at a molar ratio of Mo:Te = 1:110 and loaded into a quartz ampule. The ampule was evacuated to $\sim 10^{-5}$ Torr, subjected to multiple purge-pump cycles, and flame-sealed under vacuum. The sealed ampule was heated to 880 °C over 24 h, held for 12 h, and then slow-cooled at 1 °C/h to 530 °C. Crystals were separated from the molten flux by centrifugation at 530 °C. A subsequent post-annealing step was performed for 48 hours in a temperature gradient ($T_{\text{hot}} = 400$ °C, $\Delta T \approx 200$ °C) to remove residual tellurium and reduce tellurium inclusions, yielding high-quality MoTe₂ crystals suitable for mechanical exfoliation and 2D device fabrication.

FDU: High-purity molybdenum powders (99.997% Mo) and excess tellurium blocks (99.99999%) were thoroughly mixed at a molar ratio of 1:30 and loaded into a quartz ampule. The ampule was subsequently sealed under high vacuum ($\sim 10^{-5}$ Torr). The sealed ampule was then heated to 1000 °C over 40 hours, followed by a 168-hours dwell at 1000 °C. Then, the ampule was cooled at a rate of 1 °C/hour to 550 °C before centrifuging. To further remove the excess tellurium flux, the MoTe₂ crystals were transferred to a second vacuum-sealed ampule and subjected to a temperature-gradient ($T_{\text{hot}} = 420$ °C, $\Delta T \approx 200$ °C) with the crystals placed at the hot end for 16 hours before cooling to room temperature. This process effectively removed the excess tellurium flux, yielding high-quality MoTe₂ crystals.

Device fabrications

The triple-gated tMoTe₂ devices were fabricated following procedures similar to those reported previously [8,12,15]. Atomically thin flakes of graphite, hexagonal boron nitride (hBN), 2H-MoTe₂, and 2H-TaSe₂ were mechanically exfoliated from bulk crystals. Heterostructure assembly was carried out using a standard dry-transfer technique [66] with polycarbonate (PC) stamps inside a nitrogen-filled glove box to minimize sample degradation. The resulting stack, from top to bottom, consisted of a graphite top gate, a 10–30 nm hBN as the top dielectric layer, two pieces of few-layer TaSe₂ serving as electrical contacts to MoTe₂, twisted bilayer MoTe₂ (with the twisted angle controlled by a mechanical rotator during stacking), followed by a 10–30 nm hBN bottom dielectric layer and a graphite bottom gate. The assembled stack was released onto a Si/SiO₂ substrate with prepatterned Ti/Au/Pt (3 nm/10 nm/2 nm) electrodes. The entire stack was subsequently annealed at 300 °C for approximately 1 hour in Ar/H₂

forming gas. Device patterning into a Hall-bar geometry was then carried out using standard electron-beam lithography and reactive ion etching (CHF₃/O₂) processes.

Transport Measurements

Electrical transport measurements above 1.5 K were mainly performed in two closed-cycle ⁴He cryostats equipped with superconducting magnets. Measurements below 1.5 K were mainly performed in a cryogen free dilution refrigerator (Q-one, Q-400) equipped with a 9 T superconducting magnet. The nominal base temperature is about 10 mK. Each fridge line has a sliver epoxy filter and multiple stage RC- filters at low temperature. We performed the electrical transport measurements by using the standard low-frequency lock-in techniques. The bias current is limited within 3 nA to avoid sample heating and disturbance of fragile quantum states.

The longitudinal resistivity ρ_{xx} is obtained from the longitudinal resistance R_{xx} by $\rho_{xx} = R_{xx} \frac{W}{L}$, where W denotes the width of the Hall bar width and L represents the distance between voltage probes. The Hall resistivity ρ_{xy} is equivalent to the measured Hall resistance R_{xy} in two-dimensional case.

Calibration of twist angles

The device geometry enables independently control of the carrier density ($n = \frac{c_t V_t + c_b V_b}{e} + n_0$) and the vertical electric displacement field ($D = \frac{c_t V_t - c_b V_b}{2\epsilon_0} + D_0$) in tMoTe₂ through the application of gate voltages on top and bottom graphite gates, V_t and V_b . Here, ϵ_0 , c_t , c_b , n_0 and D_0 denote the vacuum permittivity, geometric capacitance of the top graphite gate, geometric capacitance of the bottom graphite gate, intrinsic doping and the built-in electric field, respectively. The values of c_t and c_b are calibrated through quantum oscillations measured under a perpendicular magnetic field B (Extended Data Fig. 2). The moiré hole filling factor ν_h is determined from a sequence of correlated and/or topological quantum phases with prominent ρ_{xx} and ρ_{xy} features, controlled by the V_t and V_b . The carrier density corresponding to $\nu_h = 1$ is defined as the moiré density n_M , representing the carrier density required to fill one hole per moiré unit cell. The twist angle θ and moiré wavelength a_M are then obtained from $\theta = a \sqrt{\frac{\sqrt{3}}{2}} n_M$ and $a_M = \frac{a}{\sqrt{2(1-\cos\theta)}}$, where $a = 0.353$ nm is the lattice constant of monolayer MoTe₂. The values of θ , a_M , n_M , for device 1-11 are summarized in the table shown in Extended Data Fig. 1.

Estimation of ξ and l_m

The superconducting coherence length ξ is estimated by fitting the temperature dependence of the critical perpendicular magnetic field B_c near T_c using Ginzburg–Landau relation $B_c \approx \frac{\Phi_0}{2\pi\xi^2} \left(1 - \frac{T}{T_c}\right)$, as shown in the inset of Fig. 4f. Here, $\Phi_0 = h/2e$ is the flux quantum, where h and e denote the Planck constant and elementary charge, respectively. The fitted slope yields a coherence length $\xi \approx 44$ nm.

The mean free path l_m is estimated using the two-dimensional Drude model, $l_m = \frac{h}{e^2 k_F \rho_{xx}}$, where $k_F = \sqrt{2\pi n}$ is the Fermi wave vector assuming a degeneracy of 2.

This estimation yields a mean free path $l_m \approx 120$ nm.

Continuum Model Calculations for tMoTe₂

The electronic band structures of tMoTe₂ were calculated using a continuum model. Focusing on the low-energy physics originating from the K and K' valleys of the constituent MoTe₂ monolayers, the continuum Hamiltonian \hat{H}_s for spin valley s ($s = \pm 1$ for spin up/down, locked to K/K' valleys respectively due to strong Ising-type spin-orbit coupling) is given by:

$$\hat{H}_s = \begin{bmatrix} -\frac{(\hat{\mathbf{k}} - \mathbf{K}_t)^2}{2m^*} + \Delta_+(\mathbf{r}) + \frac{\Delta_D}{2} & \Delta_T(\mathbf{r}) \\ \Delta_T^\dagger(\mathbf{r}) & -\frac{(\hat{\mathbf{k}} - \mathbf{K}_b)^2}{2m^*} + \Delta_-(\mathbf{r}) - \frac{\Delta_D}{2} \end{bmatrix} \quad (1)$$

with the moiré potentials and interlayer tunneling defined as:

$$\begin{aligned} \Delta_\pm(\mathbf{r}) &= 2V_1 \sum_{i=1,3,5} \cos(\mathbf{g}_i^1 \cdot \mathbf{r} \pm \phi_1) + 2V_2 \sum_{i=1,3,5} \cos(\mathbf{g}_i^2 \cdot \mathbf{r}) \\ \Delta_T(\mathbf{r}) &= w_1 \sum_{i=1,2,3} e^{-i\mathbf{q}_i^1 \cdot \mathbf{r}} + w_2 \sum_{i=1,2,3} e^{-i\mathbf{q}_i^2 \cdot \mathbf{r}} \end{aligned} \quad (2)$$

where $\hat{\mathbf{k}}$ is the continuous momentum operator, and \mathbf{K}_t , \mathbf{K}_b are the respective zone-corner momenta for the top and bottom monolayer, respectively. The intralayer moiré potential profiles are given by $\Delta_\pm(\mathbf{r})$, while $\Delta_T(\mathbf{r})$ represents the spatially modulated interlayer electronic hybridization. The momentum transfers \mathbf{g}_i^1 and \mathbf{g}_i^2 correspond to intralayer scattering up to the second nearest-neighbor shells in momentum space, whereas \mathbf{q}_i^1 and \mathbf{q}_i^2 dictate the interlayer scattering vectors. The effect of the applied vertical displacement electric field D is incorporated via the interlayer potential

difference term $\Delta_D = eDd/\varepsilon_{\text{MoTe}_2}$, where $d \approx 0.7$ nm is the physical interlayer distance and $\varepsilon_{\text{MoTe}_2} \approx 10$ accounts for the background dielectric constant characterizing the tMoTe₂ environment. The continuum parameters employed in our calculation are from first-principle calculation with density-dependent vdW corrections [67]: $m^* = 0.62m_e$, $V_1 = 10.3$ meV, $V_2 = 2.9$ meV, $w_1 = -7.8$ meV, $w_2 = 6.9$ meV, and $\phi_1 = -75^\circ$. The reciprocal vectors are scaled by the moiré lattice constant $L_m = a/(2\sin(\theta/2))$, where $a = 3.52$ Å is the lattice constant of monolayer MoTe₂.

To obtain the single-particle DOS map, the Hamiltonian was numerically diagonalized in the plane-wave basis truncated at a sufficient cutoff (the 5th moiré momentum shell). For high-resolution DOS mapping, the moiré Brillouin zone was sampled using a dense $N_k \times N_k$ Monkhorst-Pack mesh with $N_k = 500$ (i.e., 2.5×10^5 \mathbf{k} -points per valley).

The total DOS $DOS(\varepsilon)$ was evaluated by integrating over the full Brillouin zone for both valleys:

$$DOS(\varepsilon) = \frac{1}{\Omega_m} \sum_{s,n,\mathbf{k}} \frac{1}{\sigma\sqrt{2\pi}} \exp\left(-\frac{(\varepsilon - \varepsilon_{n,s}(\mathbf{k}))^2}{2\sigma^2}\right)$$

where $\Omega_m = \sqrt{3}L_m^2/2$ is the moiré unit cell area, n is the band index, and σ represents the artificial Gaussian broadening introduced for numerical integration. To cleanly resolve the sharp van Hove singularities characteristic of the flat bands, an adaptive broadening scheme was employed, setting $\sigma \approx w/3N_k$ where w is the bandwidth of the first moiré bands. The integration mapped the energy states into v_h to facilitate direct comparison with transport measurements.

Acknowledgements

This work is supported by National Key R&D Program of China (Nos. 2022YFA1405400, 2022YFA1402404, 2022YFA1402702, 2022YFA1403301), the National Natural Science Foundation of China (Nos. 12350403, 92565302, 12374045, 12350404, 12204115, 92265102), the Quantum Science and Technology-National Science and Technology Major Project (Nos. 2021ZD0302600, 2021ZD0302500), the Natural Science Foundation of Shanghai (No. 24LZ1401100, 24QA2703700), and the Shanghai Jiao Tong University 2030 Initiative Program. J.G. and Y. Zhang acknowledge support from the Fundamental and Interdisciplinary Disciplines Breakthrough Plan of the Ministry of Education of China, (Grant No. JYB2025XDXM120), the Shanghai Municipal Science and Technology Commission

(Grants No. 23JC1400600), and the China Postdoctoral Science Foundation (Grant No. 2022M720812). T.L. acknowledges support from the New Cornerstone Science Foundation through the XPLOER PRIZE. X.L. acknowledges “Shuguang Program” supported by Shanghai Education Development Foundation. F.X. are supported by T.D. Lee scholarship. Yang Zhang acknowledges support from AI-Tennessee and Max Planck partner lab grant. K.W. and T.T. acknowledge support from the JSPS KAKENHI (Nos. 21H05233 and 23H02052) and World Premier International Research Center Initiative (WPI), MEXT, Japan.

Reference

1. Mak, K. F. & Shan, J. Semiconductor moiré materials. *Nat. Nanotechnol.* **17**, 686–695 (2022).
2. Li, B. H., Qiu, W. X., Wu, F. C. & MacDonald, A. H. Quantum phases in twisted homobilayer transition metal dichalcogenides. *Natl. Sci. Rev.* **13** (2025).
3. Cao, T., Fu, L., Ju, L., Xiao, D. & Xu, X. Fractional Quantum Anomalous Hall Effect. *Annu. Rev. Condens. Matter Phys.* (2025).
4. Bernevig, B. A. *et al.* Fractional quantization in insulators from Hall to Chern. *Nat. Phys.* **21**, 1702–1713 (2025).
5. Cai, J. *et al.* Signatures of fractional quantum anomalous Hall states in twisted MoTe₂. *Nature* **622**, 63–68 (2023).
6. Zeng, Y. *et al.* Thermodynamic evidence of fractional Chern insulator in moiré MoTe₂. *Nature* **622**, 69–73 (2023).
7. Park, H. *et al.* Observation of fractionally quantized anomalous Hall effect. *Nature* **622**, 74–79 (2023).
8. Xu, F. *et al.* Observation of Integer and Fractional Quantum Anomalous Hall Effects in Twisted Bilayer MoTe₂. *Phys. Rev. X* **13**, 031037 (2023).
9. Ji, Z. *et al.* Local probe of bulk and edge states in a fractional Chern insulator. *Nature* **635**, 578–583 (2024).
10. Redekop, E. *et al.* Direct magnetic imaging of fractional Chern insulators in twisted MoTe₂. *Nature* **635**, 584–589 (2024).
11. Kang, K. *et al.* Evidence of the fractional quantum spin Hall effect in moiré MoTe₂. *Nature* **628**, 522–526 (2024).
12. Xu, F. *et al.* Interplay between topology and correlations in the second moiré band of twisted bilayer MoTe₂. *Nat. Phys.* **21**, 542–548 (2025).
13. Park, H. *et al.* Ferromagnetism and topology of the higher flat band in a fractional Chern insulator. *Nat. Phys.* **21**, 549–555 (2025).
14. Park, H. *et al.* Observation of dissipationless fractional Chern insulator. *Nat. Phys.* (2026).

15. Xu, F. *et al.* Signatures of unconventional superconductivity near reentrant and fractional quantum anomalous Hall insulators. arXiv:2504.06972 (2025).
16. Li, W. *et al.* Universal Magnetic Phases in Twisted Bilayer MoTe₂. *Nano Lett.* **25**, 18044–18050 (2025).
17. Anderson, E. *et al.* Trion sensing of a zero-field composite Fermi liquid. *Nature* **635**, 590–595 (2024).
18. Wang, Y. *et al.* Hidden states and dynamics of fractional fillings in twisted MoTe₂ bilayers. *Nature* **641**, 1149–1155 (2025).
19. Holtzmann, W. *et al.* Optical control of integer and fractional Chern insulators. *Nature* **649**, 1147–1152 (2026).
20. Huber, O. *et al.* Optical control over topological Chern number in moiré materials. *Nature* **649**, 1153–1158 (2026).
21. Cai, X. *et al.* Optical switching of a moiré Chern ferromagnet. *Nature* **650**, 580–584 (2026).
22. Pan, H. *et al.* Optical Signatures of $-1/3$ Fractional Quantum Anomalous Hall State in Twisted MoTe₂. *Phys. Rev. Lett.* **136**, 056601 (2026).
23. Xia, Y., Han, Z., Watanabe, K., Taniguchi, T., Shan, J. & Mak, K. F. Superconductivity in twisted bilayer WSe₂. *Nature* **637**, 833–838 (2025).
24. Guo, Y. *et al.* Superconductivity in 5.0° twisted bilayer WSe₂. *Nature* **637**, 839–845 (2025).
25. Xia, Y. *et al.* Bandwidth-tuned Mott transition and superconductivity in moiré WSe₂. *Nature* **650**, 585–591 (2026).
26. Guo, Y. *et al.* Angle evolution of the superconducting phase diagram in twisted bilayer WSe₂. arXiv:2512.06265 (2025).
27. Wu, F. C., Lovorn, T., Tutuc, E., Martin, I. & MacDonald, A. H. Topological Insulators in Twisted Transition Metal Dichalcogenide Homobilayers. *Phys. Rev. Lett.* **122**, 086402 (2019).
28. Yu, H., Chen, M. & Yao, W. Giant magnetic field from moiré induced Berry phase in homobilayer semiconductors. *Natl. Sci. Rev.* **7**, 12–20 (2020).
29. Li, H., Kumar, U., Sun, K. & Lin, S. Z. Spontaneous fractional Chern insulators in transition metal dichalcogenide moiré superlattices. *Phys. Rev. Res.* **3**, L032070 (2021).
30. Devakul, T., Crépel, V., Zhang, Y. & Fu, L. Magic in twisted transition metal dichalcogenide bilayers. *Nat. Commun.* **12**, 6730 (2021).
31. Kane, C. L., Mele, E. J. Quantum Spin Hall Effect in Graphene. *Phys. Rev. Lett.* **95**, 226801 (2005).
32. Dong, J., Wang, J., Ledwith, P. J., Vishwanath, A. & Parker, D. E. Composite Fermi Liquid at Zero Magnetic Field in Twisted MoTe₂. *Phys. Rev. Lett.* **131**, 136502 (2023).
33. Goldman, H., Reddy, A. P., Paul, N. & Fu, L. Zero-Field Composite Fermi Liquid in Twisted Semiconductor Bilayers. *Phys. Rev. Lett.* **131**, 136501 (2023).
34. Sheng, D. N., Reddy, A. P., Abouelkomsan, A., Bergholtz, E. J. & Fu, L. Quantum Anomalous Hall Crystal at Fractional Filling of Moiré Superlattices. *Phys. Rev. Lett.* **133**, 066601 (2024).

35. Stern, A. & Fu, L. Transport Properties of a Half-Filled Chern Band at the Electron and Composite Fermion Phases. *Phys. Rev. Lett.* **133**, 246602 (2024).
36. Reddy, A. P. & Fu, L. Toward a global phase diagram of the fractional quantum anomalous Hall effect. *Phys. Rev. B* **108**, 245159 (2023).
37. Muñoz-Segovia, D., Crépel, V., Queiroz, R. & Millis, A. J. Twist-angle evolution of the intervalley-coherent antiferromagnet in twisted WSe₂. *Phys. Rev. B* **112**, 085111 (2025).
38. Li, B. H., Qiu, W. X. & Wu, F. C. Electrically tuned topology and magnetism in twisted bilayer MoTe₂ at $\nu_h=1$. *Phys. Rev. B* **109**, L041106 (2024).
39. Pan, H., Wu, F. C. & Das Sarma, S. Band topology, Hubbard model, Heisenberg model, and Dzyaloshinskii-Moriya interaction in twisted bilayer WSe₂. *Phys. Rev. Res.* **2**, 033087 (2020).
40. Zang, J., Wang, J., Cano, J. & Millis, A. J. Hartree-Fock study of the moiré Hubbard model for twisted bilayer transition metal dichalcogenides. *Phys. Rev. B* **104**, 075150 (2021).
41. Hsu, Y-T., Wu, F. C. & Das Sarma, S. Spin-valley locked instabilities in moiré transition metal dichalcogenides with conventional and higher-order Van Hove singularities. *Phys. Rev. B* **104**, 195134 (2021).
42. Qiu, W.-X., Li, B., Luo, X.-J. & Wu, F. C. Interaction-Driven Topological Phase Diagram of Twisted Bilayer MoTe₂. *Phys. Rev. X* **13**, 041026 (2023).
43. Wang, T., Devakul, T., Zaletel, M. P. & Fu, L. Diverse magnetic orders and quantum anomalous Hall effect in twisted bilayer MoTe₂ and WSe₂. arXiv:2306.02501 (2024).
44. Yu, J. *et al.* Fractional Chern insulators versus nonmagnetic states in twisted bilayer MoTe₂. *Phys. Rev. B* **109**, 045147 (2024).
45. Abouelkomsan, A., Reddy, A. P., Fu, L. & Bergholtz, E. J. Band mixing in the quantum anomalous Hall regime of twisted semiconductor bilayers. *Phys. Rev. B* **109**, L121107 (2024).
46. Foutty, B. A. *et al.* Mapping twist-tuned multiband topology in bilayer WSe₂. *Science* **384**, 343–347 (2024).
47. Gao, B. *et al.* Probing Quantum Anomalous Hall States in Twisted Bilayer WSe₂ via Attractive Polaron Spectroscopy. arXiv:2504.11530 (2025).
48. Knüppel, P. *et al.* Correlated states controlled by a tunable van Hove singularity in moiré WSe₂ bilayers. *Nat. Commun.* **16**, 1959 (2025).
49. Schrade, C. & Fu, L. Nematic, chiral, and topological superconductivity in twisted transition metal dichalcogenides. *Phys. Rev. B* **110**, 035143 (2024).
50. Fischer, A. *et al.* Theory of intervalley-coherent AFM order and topological superconductivity in tWSe₂. *Phys. Rev. X* **15**, 041055 (2025).
51. Qin, W., Qiu, W.-X. & Wu, F. Topological chiral superconductivity mediated by intervalley antiferromagnetic fluctuations in twisted bilayer WSe₂. *Phys. Rev. Lett.* **135**, 246002 (2025).

52. Tuo, C., Li, M.-R., Wu, Z., Sun, W. & Yao, H. Theory of topological superconductivity and antiferromagnetic correlated insulators in twisted bilayer WSe₂. *Nat. Commun.* **16**, 9525 (2025).
53. Xie, F. *et al.* Superconductivity in Twisted WSe₂ from Topology-Induced Quantum Fluctuations. *Phys. Rev. Lett.* **134**, 136503 (2025).
54. Chubukov, A. V. & Varma, C. M. Quantum criticality and superconductivity in twisted transition metal dichalcogenides. *Phys. Rev. B* **111**, 014507 (2025).
55. Zhu, J., Chou, Y.-Z., Xie, M. & Das Sarma, S. Superconductivity in twisted transition metal dichalcogenide homobilayers. *Phys. Rev. B* **111**, L060501 (2025).
56. Kim, S., Mendez-Valderrama, J. F., Wang, X. & Chowdhury, D. Theory of correlated insulators and superconductor at $\nu = 1$ in twisted WSe₂. *Nat. Commun.* **16**, 1701 (2025).
57. Akbar, W., Biborski, A., Rademaker, L. & Zegrodnik, M. Topological superconductivity with mixed singlet-triplet pairing in moiré transition metal dichalcogenide bilayers. *Phys. Rev. B* **110**, 064516 (2024).
58. Christos, M., Bonetti, P. M. & Scheurer, M. S. Approximate Symmetries, Insulators, and Superconductivity in the Continuum-Model Description of Twisted WSe₂. *Phys. Rev. Lett.* **135**, 046503 (2025).
59. Zegrodnik, M. & Biborski, A. Mixed singlet-triplet superconducting state within the moiré t - J - U model applied to twisted bilayer WSe₂. *Phys. Rev. B* **108**, 064506 (2023).
60. Zhang, M. *et al.* Transport Evidence for Wigner Crystals in Monolayer MoTe₂. arXiv:2506.20392 (2025).
61. Fallahazad, B. *et al.* Shubnikov–de Haas Oscillations of High-Mobility Holes in Monolayer and Bilayer WSe₂: Landau Level Degeneracy, Effective Mass, and Negative Compressibility. *Phys. Rev. Lett.* **116**, 086601 (2016).
62. Pack, J. *et al.* Charge-transfer contacts for the measurement of correlated states in high-mobility WSe₂. *Nat. Nanotech.* **19**, 948–954 (2025).
63. Wang, J., Cano, J., Millis, A. J., Liu, Z. & Yang, B. Exact Landau Level Description of Geometry and Interaction in a Flatband. *Phys. Rev. Lett.* **127**, 246403 (2021).
64. Ledwith, P. J., Vishwanath, A. & Parker, D. E. Vortexability: A unifying criterion for ideal fractional Chern insulators. *Phys. Rev. B* **108**, 205144 (2023).
65. Liu, F. *et al.* From fractional Chern insulators to topological electronic crystals in moiré MoTe₂: quantum geometry tuning via remote layer. arXiv:2512.03622 (2025).
66. Wang, L. *et al.* One-dimensional electrical contact to a two-dimensional material. *Science* **342**, 614–617 (2013).
67. Mao, N. *et al.* Transfer learning relaxation, electronic structure and continuum model for twisted bilayer MoTe₂. *Commun. Phys.* **7**, 262 (2024).

Main Figures

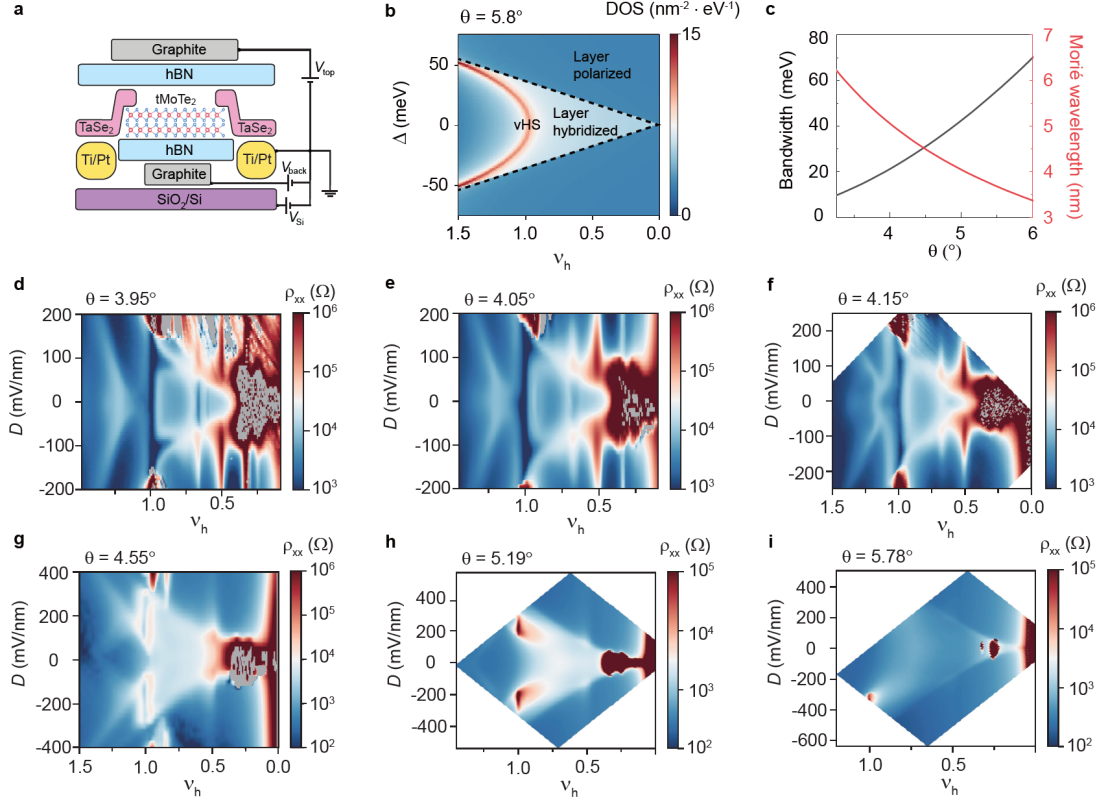


Fig. 1 | Twist-angle-dependent transport phase diagrams in tMoTe₂. **a**, Schematic illustration of the tMoTe₂ device structure used for transport measurements. **b**, Calculated DOS as a function of interlayer potential difference Δ and ν_h at $\theta = 5.8^\circ$. **c**, Calculated bandwidth (black) of the first moiré mini band and the moiré wavelength (red) as a function of θ . **d-i**, Longitudinal resistivity ρ_{xx} as a function of D and ν_h for device 2 (**d**), 3 (**e**), 4 (**f**), 6 (**g**), 10 (**h**), and 11 (**i**) at $T = 1.6$ K, with θ ranging from 3.95° to 5.78° . Panel **d-g** were measured under a small perpendicular magnetic field $B = 0.1$ T, whereas panel **h** and **i** were measured at $B = 0$. Grey regions indicate areas inaccessible to electrical transport measurements due to extremely large sample resistance or poor electrical contacts.

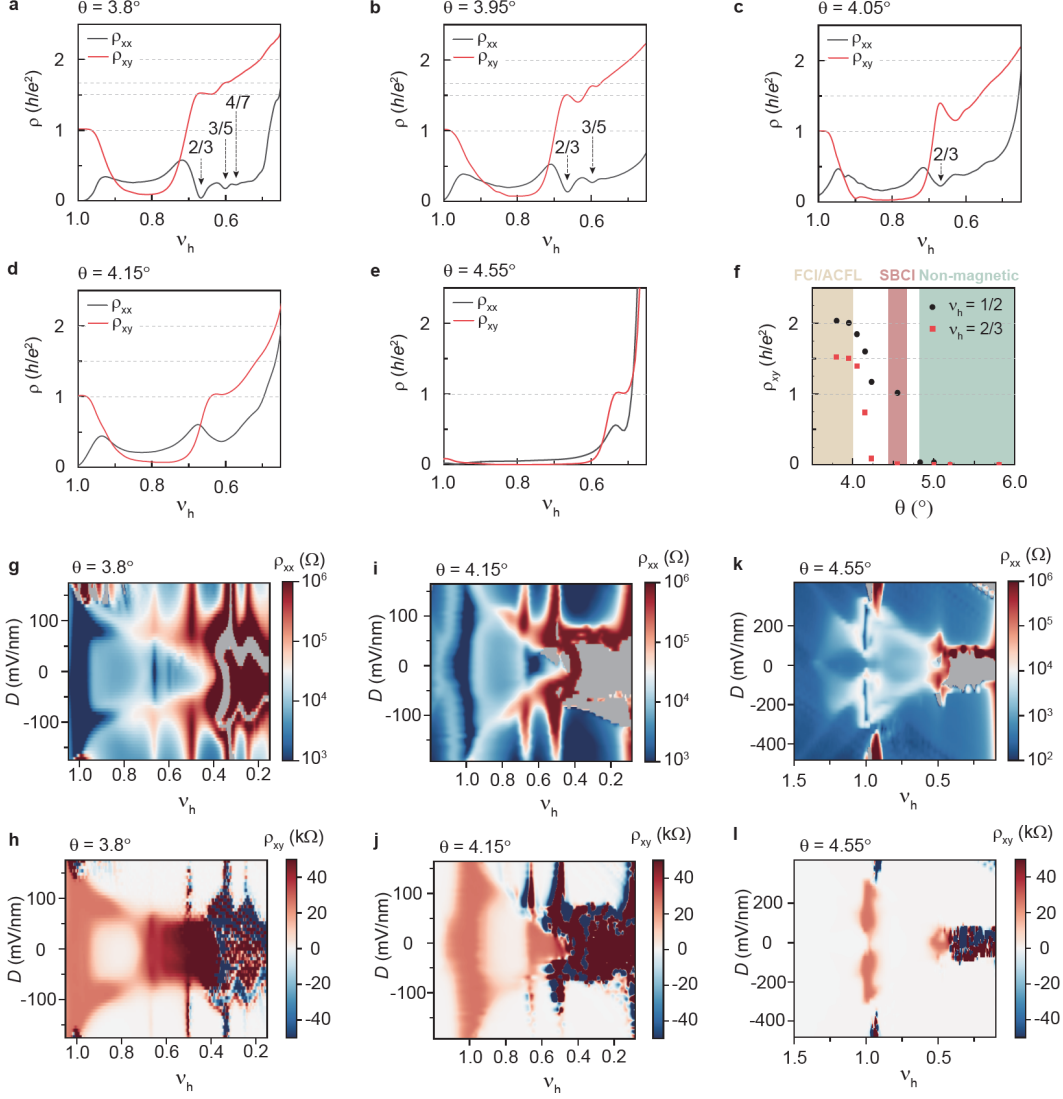


Fig. 2 | The evolution of fractional topological phases with twist angles. **a-e**, Symmetrized ρ_{xx} and antisymmetrized ρ_{xy} as a function of ν_h for device 1 (**a**), 2 (**b**), 3 (**c**), 4 (**d**), and 6 (**e**) measured at $B = 0.1$ T, with θ ranging from 3.8° to 4.55° . Panel **a-d** were measured at $T = 1.6$ K, whereas panel **e** was measured at $T = 0.3$ K due to the lower Curie temperature at larger θ . **f**, Antisymmetrized ρ_{xy} at $B = 0.1$ T as a function of θ at $\nu_h = 2/3$ and $1/2$. For devices exhibiting ferromagnetism ($\theta < 4.83^\circ$), the ρ_{xy} shown in **f** reflects the anomalous Hall response. **g,h** Symmetrized ρ_{xx} (**g**) and antisymmetrized ρ_{xy} (**h**) as a function of ν_h and D for device 1 (3.8°), measured at $T = 1.6$ K and $B = 0.1$ T. Three FQAH states are identified at $\nu_h = 2/3, 3/5$, and $4/7$. **i,j** Symmetrized ρ_{xx} (**i**) and antisymmetrized ρ_{xy} (**j**) as a function of ν_h and D for device 4 (4.15°), measured at $T = 0.6$ K and $B = 0.1$ T. Integer quantized ρ_{xy} of h/e^2 , accompanied by vanishing ρ_{xx} , is observed near $\nu_h \approx 0.62$. **k,l** Symmetrized ρ_{xx} (**k**) and antisymmetrized ρ_{xy} (**l**) as a function of ν_h and D for device 5 (4.55°), measured at $T = 0.3$ K and $B = 0.3$ T. The integer QAH state is absent at $D = 0$ but persists at $|D| \approx 100\text{-}300$ mV/nm within the layer-hybridized regime. A symmetry-broken Chern insulating state is observed at $\nu_h = 1/2$, characterized by integer-quantized ρ_{xy} and a local minimum in ρ_{xx} . Grey regions in **g, i, k** indicate areas inaccessible to electrical transport measurements due to extremely large sample resistance or poor electrical contacts.

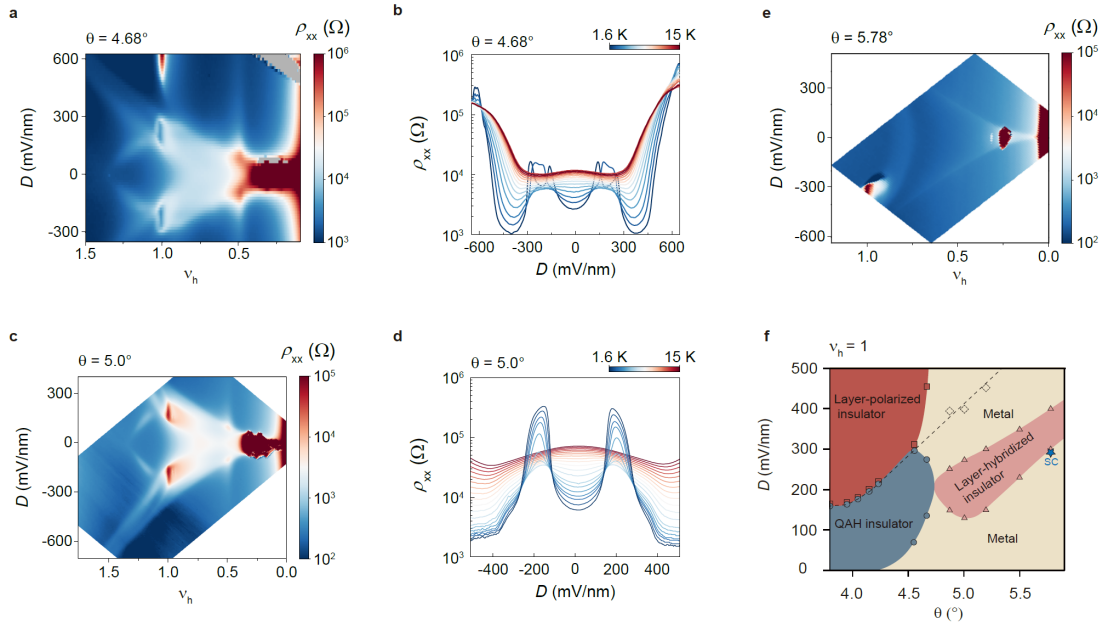


Fig. 3 | Topological and correlated phases at $\nu_h = 1$. **a**, ρ_{xx} as a function of ν_h and D for device 7 (4.68°), measured at $T = 1.6$ K and $B = 0$. **b**, Temperature-dependent ρ_{xx} as a function of D at $\nu_h = 1$ for device 7 (4.68°) at $B = 0$. **c,d**, Same as panels **a** and **b**, respectively, but measured in device 9 (5.0°). **e**, ρ_{xx} as a function of ν_h and D for device 11 (5.78°), measured at $T = 10$ mK and $B = 0$. **f**, θ - D phase diagram at $\nu_h = 1$ constructed from experimental data (symbols). Dark red denotes the layer-polarized insulator, dark blue the QAH insulator, pink the layer-hybridized insulator, yellow the metallic phase, and blue star represents superconducting phase. The dashed line marks the boundary between the layer-polarized and the layer-hybridized region.

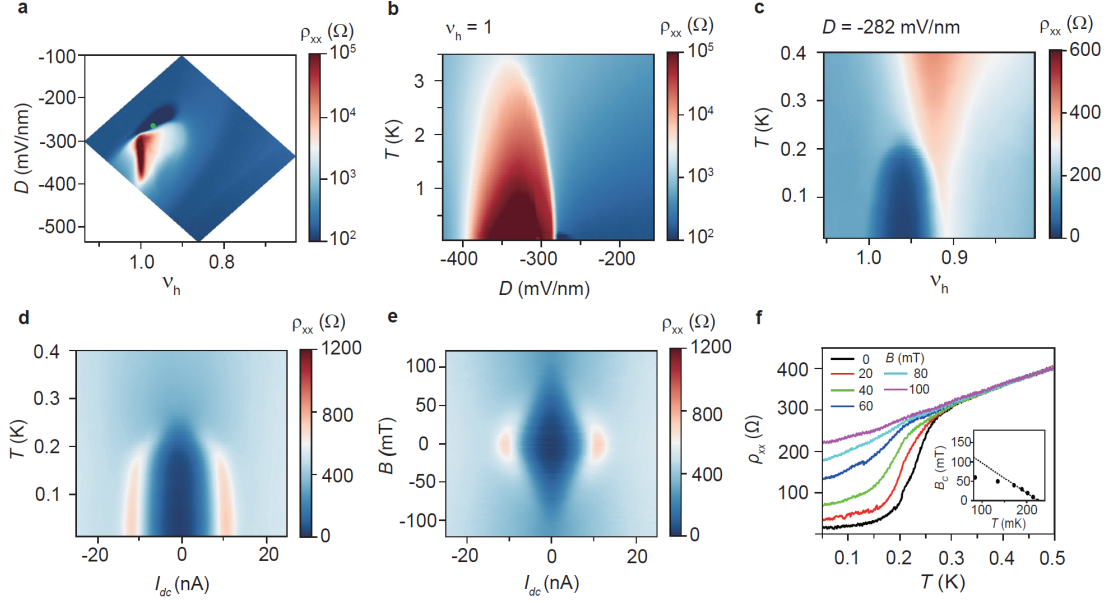
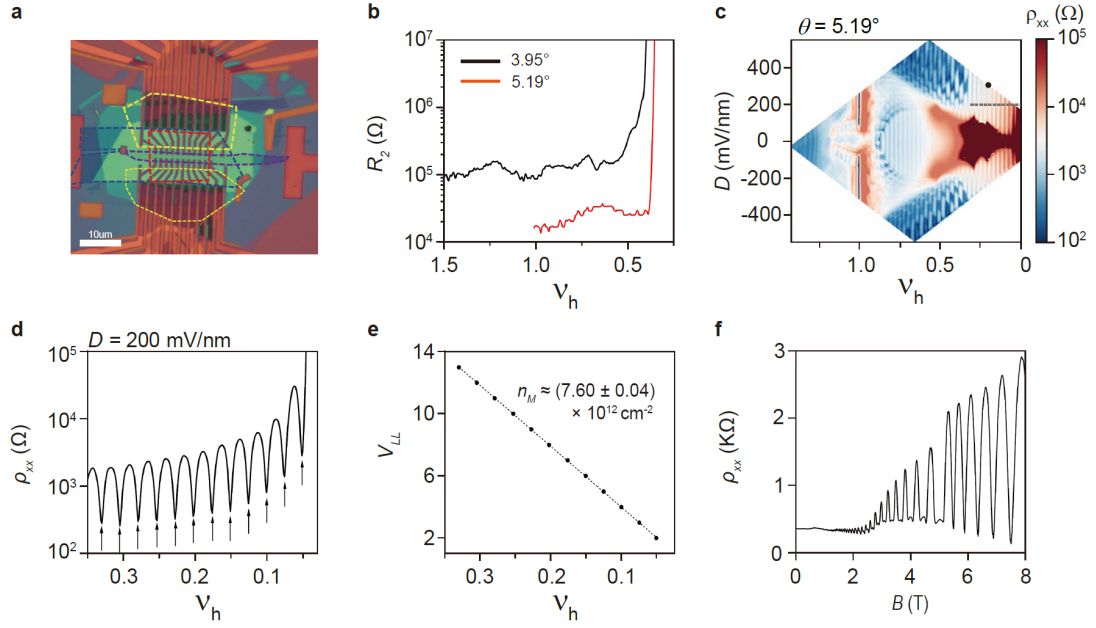


Fig. 4 | Superconductivity in 5.78° tMoTe₂. **a**, Local ρ_{xx} map as a function of ν_h and D for device 11 (5.78°), measured at $T = 10$ mK and $B = 0$. **b**, ρ_{xx} as a function of T and D at $\nu_h = 1$. **c**, ρ_{xx} as a function of T and ν_h at $D = -282$ mV/nm. **d**, Differential resistivity dV/dI as a function of I_{dc} and T at $B = 0$ for the superconducting state. **e**, The $B-dV/dI-I_{dc}$ map measured at $T = 10$ mK. **f**, ρ_{xx} as a function of T under different B . The inset show the superconducting critical perpendicular magnetic field B_c as a function of T . The dashed line represents the linear fit to the data points above 150 mK. Measurements in panels **d-f** were performed at the optimal superconducting condition ($\nu_h = 0.96$, $D = -288$ mV/nm), as marked by the green dot in **a**.

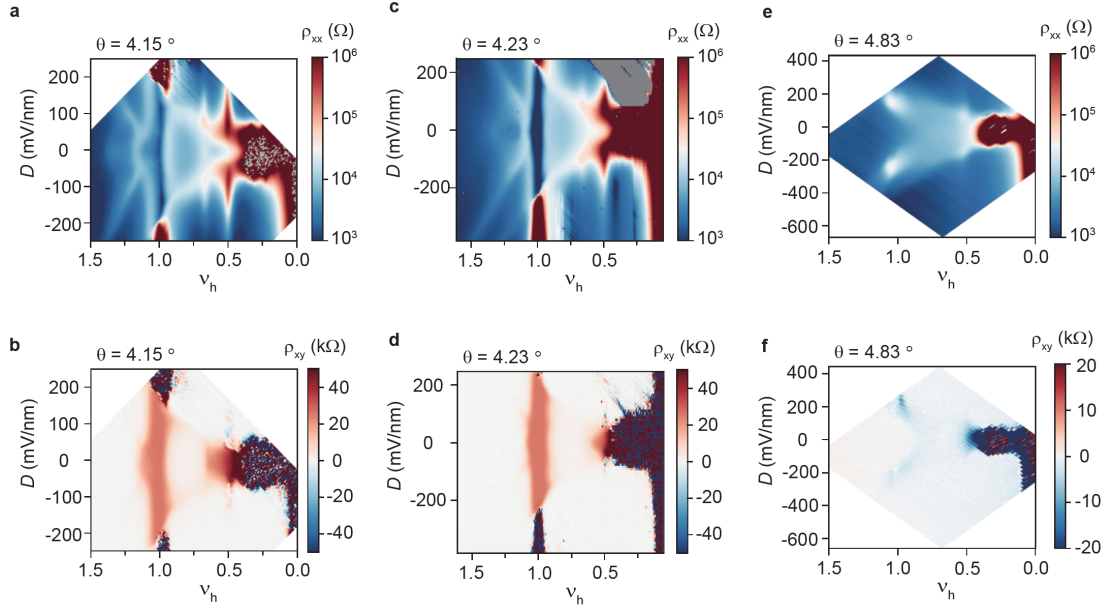
Extended Data Figures

Device	Bulk crystal	Twist angle (degree)	Moiré wavelength (nm)	Moiré density (10^{12} cm^{-2})	FCI/ACFL	IQAH
D1	HKUST	3.80 ± 0.03	5.32	4.08	Y	Y
D2	HKUST	3.95 ± 0.02	5.12	4.40	Y	Y
D3	FDU	4.05 ± 0.02	4.99	4.63	Y	Y
D4	FDU	4.15 ± 0.02	4.87	4.86	N	Y
D5	HKUST	4.23 ± 0.02	4.79	5.04	N	Y
D6	FDU	4.55 ± 0.03	4.44	5.85	N	Y
D7	FDU	4.68 ± 0.02	4.35	6.11	N	Y
D8	HKUST	4.83 ± 0.04	4.19	6.59	N	N
D9	HQ graphene	5.00 ± 0.02	4.05	7.06	N	N
D10	HKUST	5.19 ± 0.01	3.90	7.60	N	N
D11	HKUST	5.78 ± 0.02	3.50	9.42	N	N

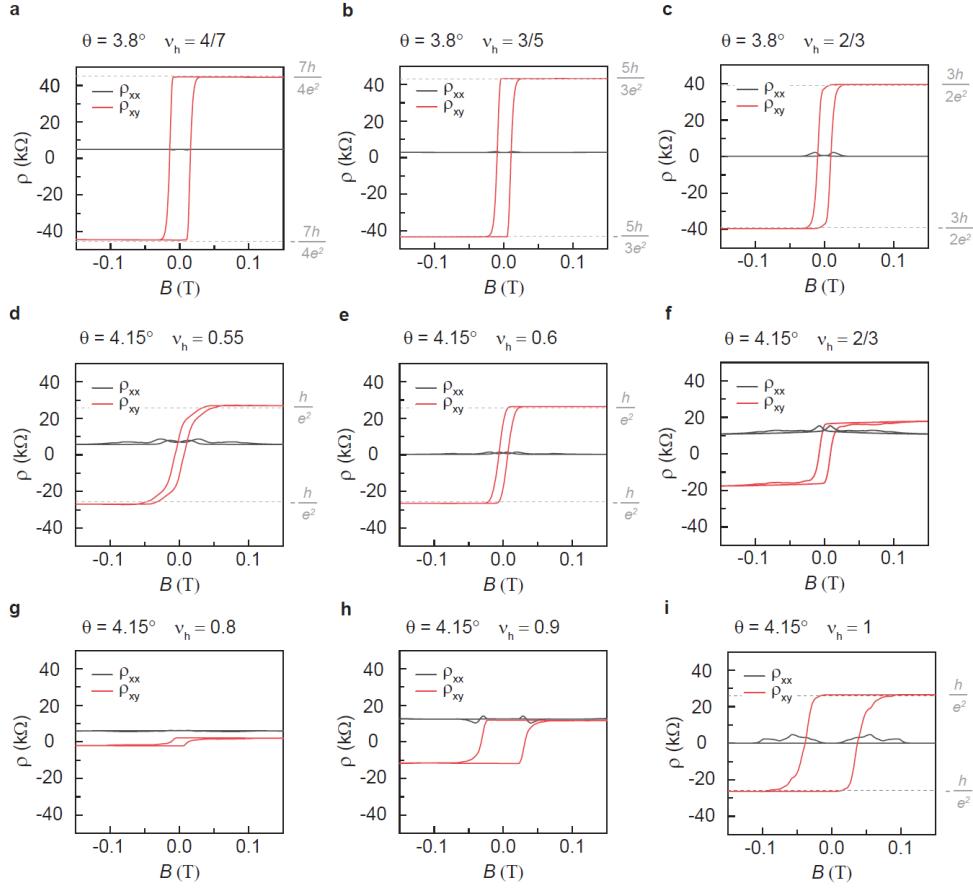
Extended Data Fig. 1. Device summary table.



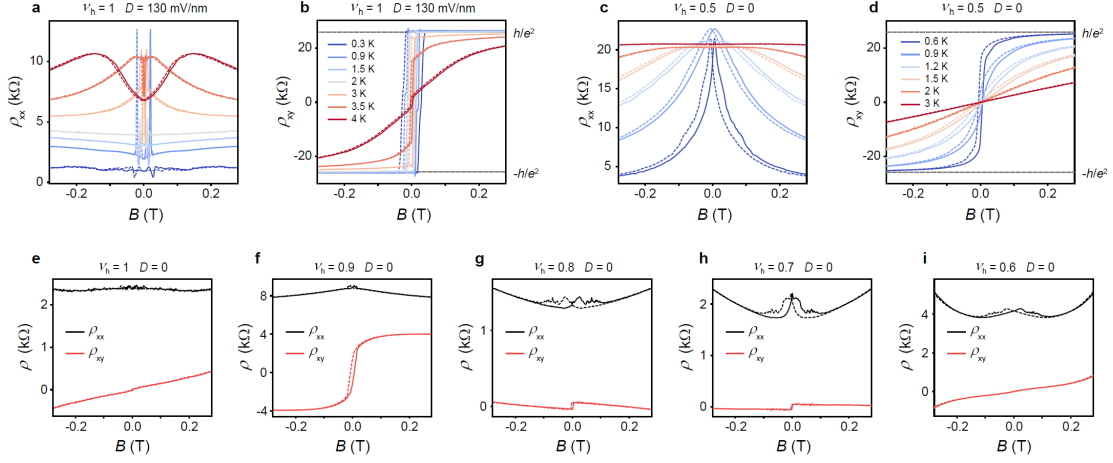
Extended Data Fig. 2. | Device image and twist angle calibration. **a**, Optical micrograph image of device 11 (5.78°). Yellow dashed lines indicate the TaSe₂ contacts. Red dashed lines outline the tMoTe₂ region. Blue and purple dashed lines denote the top-gate and bottom-gate regions, respectively. **b**, Two-terminal resistance R_2 as a function of v_h for device 2 (3.95°) and device 10 (5.19°), shown by the black and red curves, respectively. The measured R_2 is primarily limited by contact resistance. In general, devices with larger twist angles exhibit better contacts, possibly due to the less flat moiré bands. **c**, Map of ρ_{xx} as a function of v_h and D for device 10 (5.19°) measured at $T = 10$ mK and $B = 8$ T. **d**, Line cut of the data in **c** along the dashed line. **e**, Linear fit of the Landau-level filling factor ν_{LL} a function of v_h , from which the moiré density n_M is extracted. **f**, ρ_{xx} as a function of B at $D = 290$ mV/nm and $v_h = 0.25$, corresponding to the black dot marked in **c**. The onset of Shubnikov–de Haas oscillations occurs at about $B = 1.2$ T, reflecting the high quality of the device.



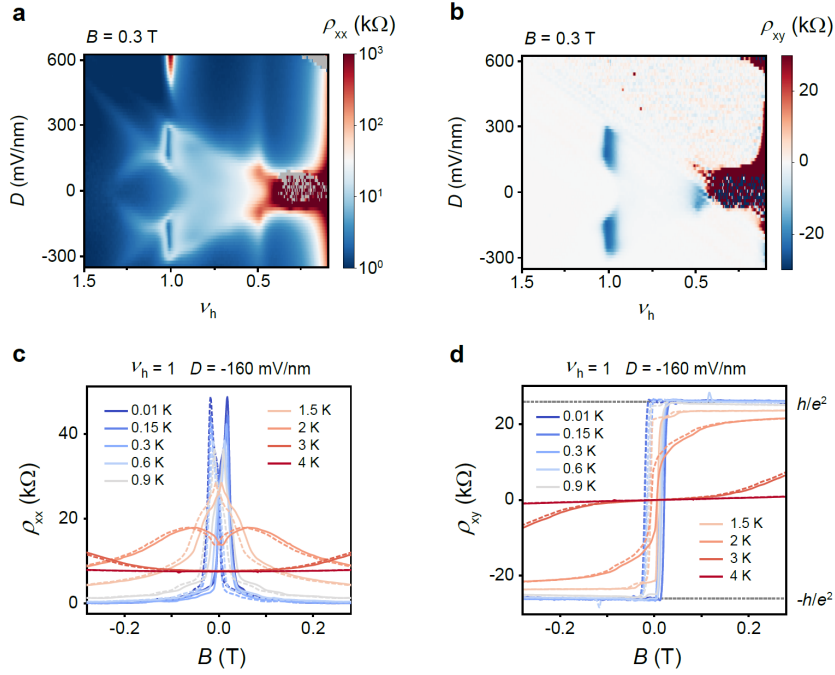
Extended Data Fig. 3. | Transport phase diagrams of device 4 (4.15°), device 5 (4.23°), and device 8 (4.83°). **a,c,e**, Symmetrized ρ_{xx} as a function of D and ν_h for device 4 (**a**), 5 (**c**), and 8 (**e**). **b,d,f**, Antisymmetrized ρ_{xy} as a function of D and ν_h for device 4 (**b**), 5 (**d**), and 8 (**f**). All maps measured at $T = 1.6$ K and with $B = 0.1$ T (**a-d**) or 0.3 T (**e,f**). Unlike devices with twist angles below 4° , which host multiple FQAH states, only IQAH states can be observed in device 4 (4.15°) and 5 (4.23°). No anomalous Hall effects and magnetic hysteresis can be observed in device 8 (4.83°).



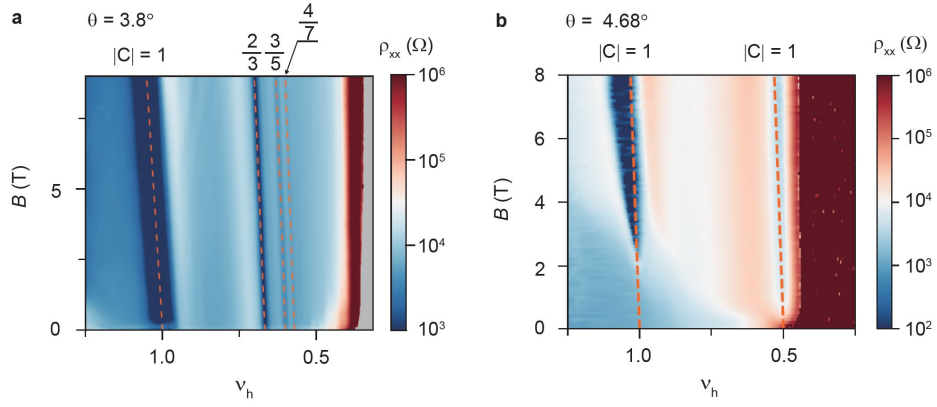
Extended Data Fig. 4. | Magnetism and Chern insulators in device 1 (3.8°) and device 4 (4.15°). **a-c**, Magnetic hysteresis loop scans at $\nu_h = 4/7$, $3/5$, and $2/3$, respectively, measured at $D = 0$ for device 1. Clear fractional quantum anomalous Hall effects are observed at these fillings. **d-i**, Magnetic hysteresis loop scans at $\nu_h = 0.55$, 0.6 , 0.67 , 0.8 , 0.9 and 1 , respectively, measured at $D = 0$ for device 4. In this device, robust ferromagnetism persists over the filling range of $\nu_h \approx 1/2$ to 1 at $D = 0$, and integer quantum anomalous Hall effects are observed at both $\nu_h = 1$ and $\nu_h \approx 0.62$. All data were acquired at $T = 600$ mK.



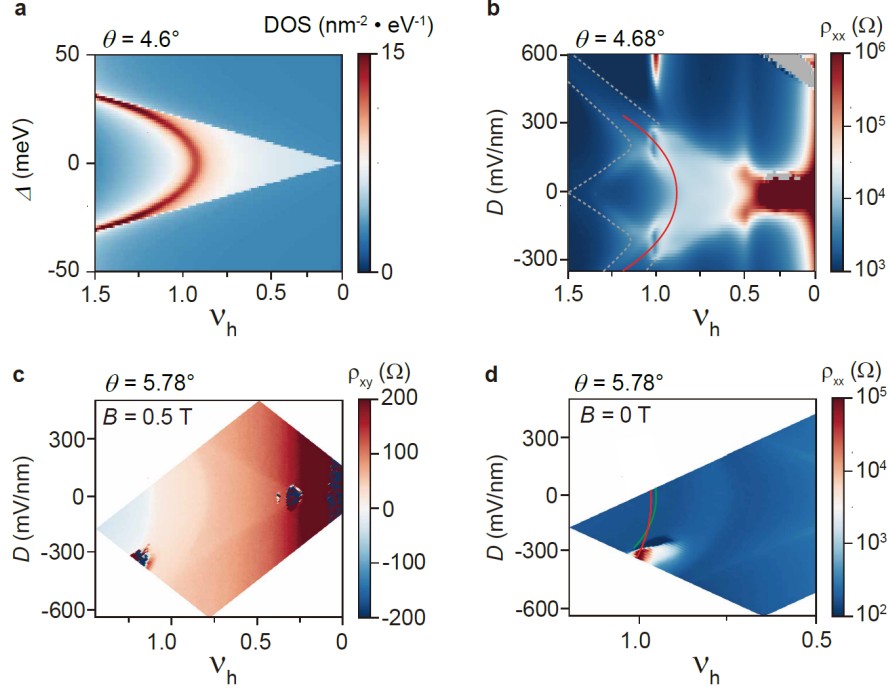
Extended Data Fig. 5. | Magnetism and Chern insulators in device 6 (4.55°). **a,b**, Temperature dependence of magnetic hysteresis loop scans of ρ_{xx} (**a**) and ρ_{xy} (**b**) at $\nu_h = 1$ and $D = 130$ mV/nm. Integer quantum anomalous Hall effect is observed at low temperatures and at $B = 0$. The Curie temperature for the ferromagnetism at $\nu_h = 1$ is approximately 4 K. **c,d**, The same as **a** and **b**, respectively, but at $\nu_h = 1/2$ and $D = 0$. Clear magnetic hysteresis loop is observed at low temperatures, but zero-field quantization is not achieved. A small magnetic field $B \approx 0.2$ T is required to stabilize the symmetry-broken Chern insulating state. The Curie temperature at $\nu_h = 1/2$ is approximately 2 K. **e-i**, Magnetic hysteresis loop scans at $\nu_h = 1, 0.9, 0.8, 0.7,$ and 0.6 , respectively, measured at $T = 300$ mK and $D = 0$, respectively. Ferromagnetism is absent around $\nu_h = 1$ and 0.6 at $D = 0$.



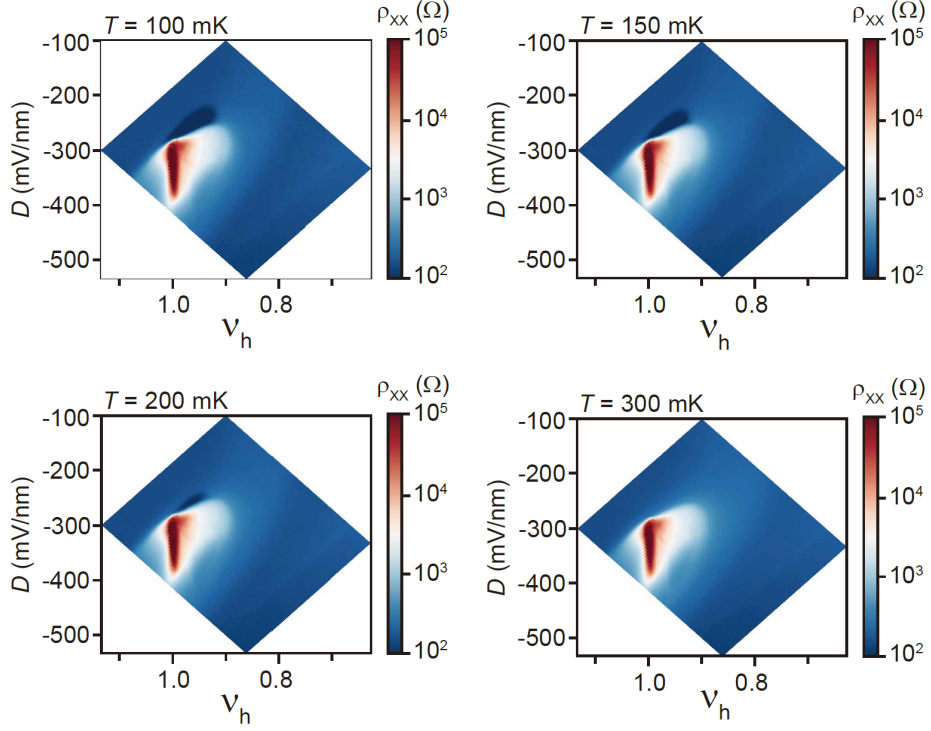
Extended Data Fig. 6. | Magnetism and Chern insulators in device 7 (4.68°). **a,b**, ρ_{xx} (**a**) and ρ_{xy} (**b**) as a function of ν_h and D at $B = 0.3$ T and $T = 1.6$ K. The IQAH state at $\nu_h = 1$ emerges only at finite D . Among fractional fillings, the anomalous Hall signal is strongest around $\nu_h = 1/2$. In this device, the symmetry-broken insulating state can be stabilized under $B \approx 0.5$ T at lower temperatures, as shown in Extended Data Fig. 7. **c,d**, Temperature dependence of magnetic hysteresis loops of ρ_{xx} (**c**) and ρ_{xy} (**d**) at $\nu_h = 1$ and $D = -160$ mV/nm. Integer quantum anomalous Hall effect is observed at low temperatures and at $B = 0$. The Curie temperature of the ferromagnetism at $\nu_h = 1$ is approximately 3 K.



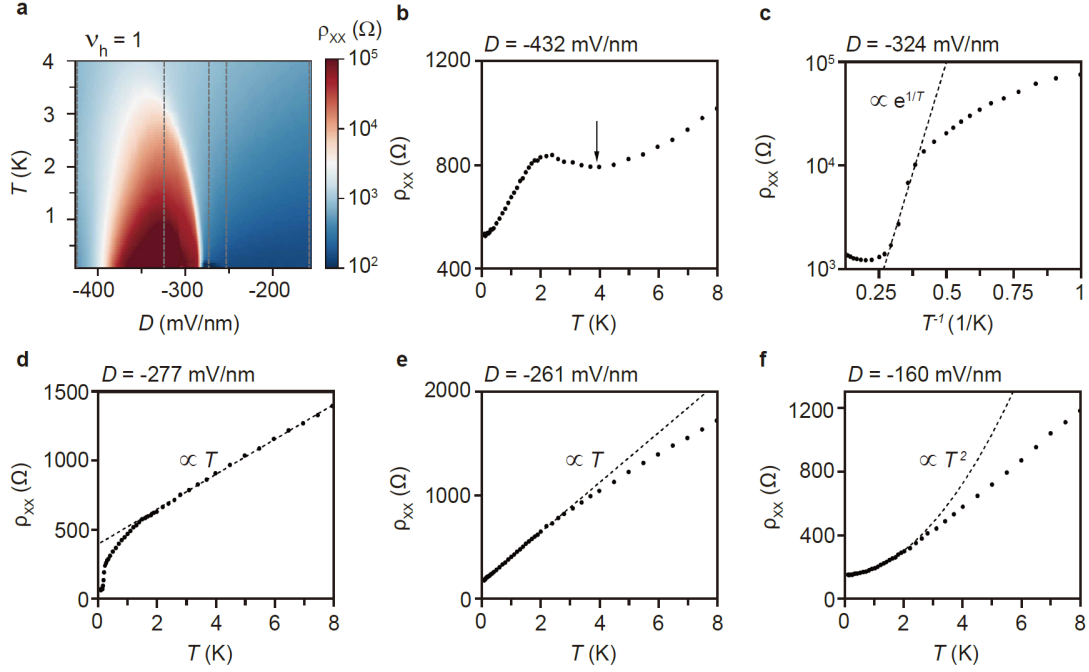
Extended Data Fig. 7. | Středa formula for integer, fractional, and symmetry-broken Chern insulators. a-b, ρ_{xx} as a function of ν_h and B for device 1 (**a**) and device 7 (**b**). Panel **a** was measured at 1.6 K and Panel **b** at 0.3 K. In device 1 (3.8°), the integer and fractional Chern insulators follows the expected dispersions based on the Středa formula $n_M \frac{d\nu_h}{dB} = C \frac{e}{h}$, as indicated by the orange dashed lines. In device 7 (4.68°), the symmetry-broken insulating states at $\nu_h = 1/2$ also approximately follows the Streda formula with $C = 1$, consistent with the measured quantized ρ_{xy} of h/e^2 .



Extended Data Fig. 8. | Calculated DOS compared with experiments. a, Calculated DOS as a function of interlayer potential difference Δ and ν_h at $\theta = 4.6^\circ$. **b**, ρ_{xx} as a function of ν_h and D at zero magnetic field for device 7 (4.68°), the same dataset as shown in Fig. 3a. The red solid line marks the calculated VHS from **a**. We approximately convert Δ into D using $D = E\varepsilon_{\text{hBN}} = \Delta\varepsilon_{\text{MoTe}_2}/(ed)$, where d is the interlayer separation in MoTe_2 , and ε_{hBN} , $\varepsilon_{\text{MoTe}_2}$ are the dielectric constant for hBN and MoTe_2 , respectively (Methods). It illustrates that the emergence of the IQAH state roughly coincides with the D -field at which the VHS crosses $\nu_h = 1$. Dashed lines mark the local ρ_{xx} peaks beyond single-particle VHS, which is likely associated with interaction-induced Fermi-surface reconstruction. **c**, Antisymmetrized ρ_{xy} as a function of ν_h and D at $B = 0.5$ T and $T = 10$ mK for device 11 (5.78°), from which the VHS position can be estimated by following the $\rho_{xy} = 0$ line. **d**, Comparison between the calculated VHS (red) and the experimentally extracted VHS from **c** (green), shown on the ρ_{xy} - ν_h - D map at $B = 0$ T and $T = 10$ mK. The calculated VHS across the superconducting and correlated insulating states, also agree reasonably well with the experimentally extracted VHS.



Extended Data Fig. 9. | T -dependent ρ_{xx} maps in device 11 (5.78°). a-d, Maps of ρ_{xx} at zero magnetic field as a function of ν_h and D , measured at $T = 100$ mK, 150 mK, 200 mK, 300 mK, respectively. Observed superconductivity is most robust at fillings slightly below $\nu_h = 1$, adjacent to the $\nu_h = 1$ correlated insulator.



Extended Data Fig. 10. | D -dependent transport behaviors at $\nu_h = 1$ in device 11 (5.78°). **a**, ρ_{xx} as a function of T and D at zero magnetic field for the 5.78 device, the same dataset as shown in Fig. 4b. Line cuts shown in **b-f** are indicated by the vertical dashed lines. **b**, ρ_{xx} as a function of T at $D = -432$ mV/nm. A non-monotonic temperature dependence is observed, with a local ρ_{xx} minimum around 4 K. Similar behaviors have been reported in tWSe₂ [25], where the local ρ_{xx} minimum roughly indicate the Néel temperature of the valley-coherent antiferromagnetic order. **c**, ρ_{xx} as a function of $1/T$ at $D = -324$ mV/nm. Thermal activation behavior corresponding to a correlated insulator gap is observed. The fit yields a gap of ~ 2 meV. **d-f**, ρ_{xx} as a function of T at $D = -277$, -261 , and -160 mV/nm, respectively. Strange-metal behaviors with linear-in- T resistivity are observed in the superconducting normal state (**d**) and adjacent to the superconducting region (**e**). Away from the superconducting region at smaller D , Fermi liquid behaviors are observed at low temperatures (**f**).